

## Research Article

# ZnO Nanocrystals as Anode Electrodes for Lithium-Ion Batteries

Wenhui Zhang,<sup>1</sup> Lijuan Du,<sup>1</sup> Zongren Chen,<sup>1</sup> Juan Hong,<sup>2</sup> and Lu Yue<sup>1</sup>

<sup>1</sup>Jiangsu Collaborative Innovation Center for Ecological Building Materials and Environmental Protection Equipments, Key Laboratory for Advanced Technology in Environmental Protection of Jiangsu Province, Yancheng Institute of Technology, Yancheng 224051, China

<sup>2</sup>College of Mechanical Engineering, Yancheng Institute of Technology, Yancheng 224051, China

Correspondence should be addressed to Juan Hong; jameshong@ycit.cn and Lu Yue; yuelu66@126.com

Received 8 March 2016; Accepted 24 April 2016

Academic Editor: Gongming Wang

Copyright © 2016 Wenhui Zhang et al. This is an open access article distributed under the Creative Commons Attribution License, which permits unrestricted use, distribution, and reproduction in any medium, provided the original work is properly cited.

ZnO nanocrystals were synthesized via a thermal decomposition method. X-ray diffraction, transmission electron microscopy, and photoluminescence were used to investigate the composition and nanostructure of the material. Compared with commercial ZnO nanoparticles, ZnO nanocrystals showed higher lithium storage capacity and better cycling characteristics and exhibited a reversible discharge capacity of 500 mAh g<sup>-1</sup> after 100 cycles at 200 mA g<sup>-1</sup>.

## 1. Introduction

Transition metal oxides have gained more and more interest as electrode materials in lithium-ion batteries in the last decades because of their higher theoretical capacity and safety compared with the conventional carbon materials [1–4]. Among them, ZnO, a wide-bandgap semiconductor of 3.37 eV at room temperature with large exciton binding energy of 60 meV, is a multifunctional material for a variety of practical applications such as piezoelectric devices [5], field emission [6], gas sensors [7], dye-sensitized solar cells [8], and photocatalysts [9] due to its excellent physical and chemical properties. ZnO has superior advantages such as low cost, facile preparation, morphologic diversity, and high chemical stability. ZnO nanocrystals with different morphologies have some special properties of physics, so intense interests have been devoted to the synthesis of ZnO with various morphologies such as nanowires [10], nanobelts [11], nanorods [12], and nanosheets [13].

As an anode material of lithium-ion batteries, ZnO has a theoretical capacity of 978 mAh g<sup>-1</sup> [14]. However, the poor electronic conductivity, large volume change during lithium/delithium process, and the resulting severe capacity fading hinder its practical application [15]. Hitherto, some efforts have been made to improve its cycling performance including synthesis of nanostructures [15–17], doping and

forming composite with metal [18, 19], metal oxide [20–22], carbon [23, 24], and graphene [25, 26]. For example, dandelion-like ZnO nanorod arrays showed higher lithium storage capacity and better cycling characteristics compared to powder-form ZnO [27]. Mesoporous ZnO nanosheets exhibit a 50th charge capacity of 420 mAh g<sup>-1</sup>, and the capacity and cycling performance are enhanced compared with those of common solid ZnO particles [17]. More significant research efforts are needed to further improve the lithium-ion battery performances of ZnO.

In the present work, ZnO nanocrystals have been prepared by a thermal decomposition method and their electrochemical performances as lithium anode materials are investigated.

## 2. Experimental Section

**2.1. Preparation of ZnO Nanocrystals.** 0.316 g zinc stearate (Zn(St)<sub>2</sub>, 10–12% Zn basis, Sigma-Aldrich) and 10 g 1-octadecene (ODE, technical grade, 90%, Sigma-Aldrich) were loaded in a 50 mL three-necked flask, degassed, and heated to 270°C under an argon flow. A separate solution of 2.5 g ODE containing 0.676 g 1-octadecanol (ODA, 95%, Sigma-Aldrich) at 200°C was rapidly injected into the reaction flask to generate nanocrystals. The reaction was allowed

to proceed for 30 min. When the reaction was finished, the reaction mixture was cooled to room temperature. The resulting nanocrystals were precipitated out by adding ethyl acetate, carefully purified with hexane/ethanol mixtures, and dried at 70°C. Ethyl acetate (AR), hexane (AR), and ethanol (AR) were purchased from Sinopharm Chemical Reagent Co. Commercial ZnO nanoparticles (30 ± 10 nm) were purchased from Aladdin Industrial Corporation for comparison.

**2.2. Characterization of ZnO Nanocrystals.** Powder X-ray diffraction (XRD) analyses were performed on a Philips PW-1830 X-ray diffractometer with Cu K $\alpha$  irradiation ( $\lambda = 1.5406 \text{ \AA}$ ) at a scanning speed of 0.014°/sec over the  $2\theta$  range of 30–60°. The electronic morphology of the samples was examined by a transmission electron microscope (TEM; FEI Tecnaï G2 Spirit, USA). Photoluminescence (PL) spectra of the sample on Si substrate were recorded using Jobin-Yvon LabRAM high-resolution spectrometer with He-Cd laser ( $\lambda = 325 \text{ nm}$ ). Cyclic voltammetry (CV) and electrochemical impedance spectroscopy (EIS) results were obtained with Zennium/IM6 electrochemical workstation (Zahner, Germany).

**2.3. Electrochemical Performance.** The coin cells (CR2025) were assembled to test the electrochemical performance of the as-prepared electrodes. The as-prepared samples were mixed with acetylene black and carboxymethyl cellulose, in a weight ratio of 60:20:20 in an aqueous solution to form homogeneous slurry. The slurry was spread onto 10  $\mu\text{m}$  thick copper foil and dried at 60°C for 12 h in a vacuum oven and then pressed to obtain the electrode sheet with a 9–10  $\mu\text{m}$  coating thickness and a loading level of about 1.4  $\text{mg cm}^{-2}$ . The electrolyte of 1 M LiPF<sub>6</sub> and 5% fluoroethylene carbonate (FEC) in ethylene carbonate (EC, >99.9%)/diethylene carbonate (DEC, >99.9%)/dimethyl carbonate (DMC, >99.9%) (v:v:v = 1:1:1, water content <20 ppm) was purchased from Zhangjiagang Guotai-Huarong New Chemical Materials Company (China). The cells were assembled in an Ar filled glove-box. The cells were charged and discharged galvanostatically in the fixed voltage window from 0.01 V to 3 V on a Shenzhen Neware battery cycler (China) at 25°C.

EIS was measured by applying an alternating voltage of 5 mV over the frequency ranging from 10<sup>-2</sup> to 10<sup>5</sup> Hz. In this work, unless otherwise specified, all impedance measurements were carried out after one cycle of the prepared electrode.

### 3. Results and Discussion

The crystal structure of the sample was characterized by XRD, as shown in Figure 1. All diffraction peaks can be indexed as the hexagonal phase of ZnO, which is in good agreement with JCPDS number 36-1451.

The typical morphology of ZnO nanocrystals and commercial ZnO nanoparticles, as observed by TEM, is presented in Figure 2. It can be seen that the reaction generated trigonal ZnO nanocrystals with the size of 10–15 nm (side-edge length). The diameter of commercial ZnO nanoparticles was 30 ± 10 nm.

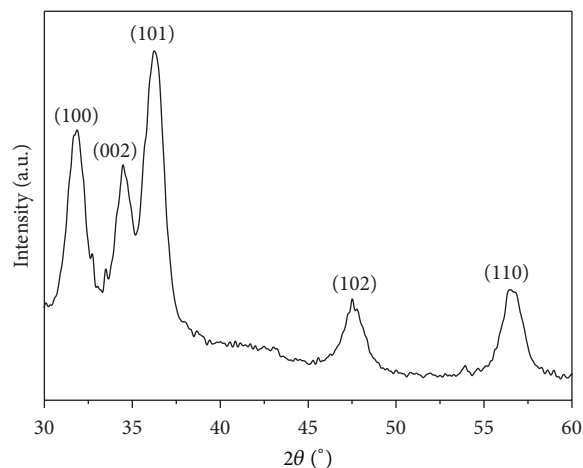


FIGURE 1: XRD pattern of ZnO nanocrystals.

PL spectrum of the sample is shown in Figure 3. Strong excitonic emission at 375 nm and a broad but weak spectral band ranging from 450 to 600 nm were observed. The near-UV peak is due to the recombination of electron and hole in an exciton, while the visible emission is due to the presence of various point defects, such as interstitial oxygen and oxygen vacancies.

The electrochemical properties of ZnO nanocrystal and commercial ZnO nanoparticle electrode for lithium-ion batteries were investigated. Figure 4 reveals the CV of the electrodes at a scan rate of 0.5  $\text{mV s}^{-1}$  in the voltage ranging from 0.01 to 3 V. Both of the first discharge process (negative scan) of ZnO nanocrystal and the commercial ZnO electrodes showed broad peaks around 1.2–1.0 V and 0.5–0.7 V and a sharp reduction peak below 0.3 V, corresponding to the irreversible reactions (the reaction of FEC decomposition and formation of primal solid electrolyte interface (SEI) film on the surface of composite electrode) and the insertion of Li ions into ZnO, respectively. The relative peak at 0.5 V originated from the reduction of ZnO into Zn and the formation of amorphous Li<sub>2</sub>O, while the strong peak near 0.25 V was caused by the generation of Li-Zn alloy together with the decomposition of electrolyte. These peaks disappeared in further cycles, indicating the irreversible reduction of ZnO with a large irreversible capacity in the first cycle. New reduction peaks at about 0.80 and 0.30 V appeared after the first cycle and shifted to a lower voltage during further cycles. In the subsequent delithium process for ZnO nanocrystals (Figure 4(a)), six weak oxidation peaks centred at 0.27, 0.52, 0.63, 1.48, 1.78, and 2.20 V could be carefully discerned which could be attributed to multistep dealloying of Li-Zn alloy. However, for commercial ZnO electrode (Figure 4(b)), only two oxidation peaks of 0.65 and 1.52 V could be found in the CV curves. Besides, the ZnO nanocrystal electrode displayed a higher peak current in both oxidation-reduction reaction processes, indicating that a better and more active electrode reaction happened.

The cycling performances of ZnO nanocrystal and commercial ZnO nanoparticle electrode at a current density

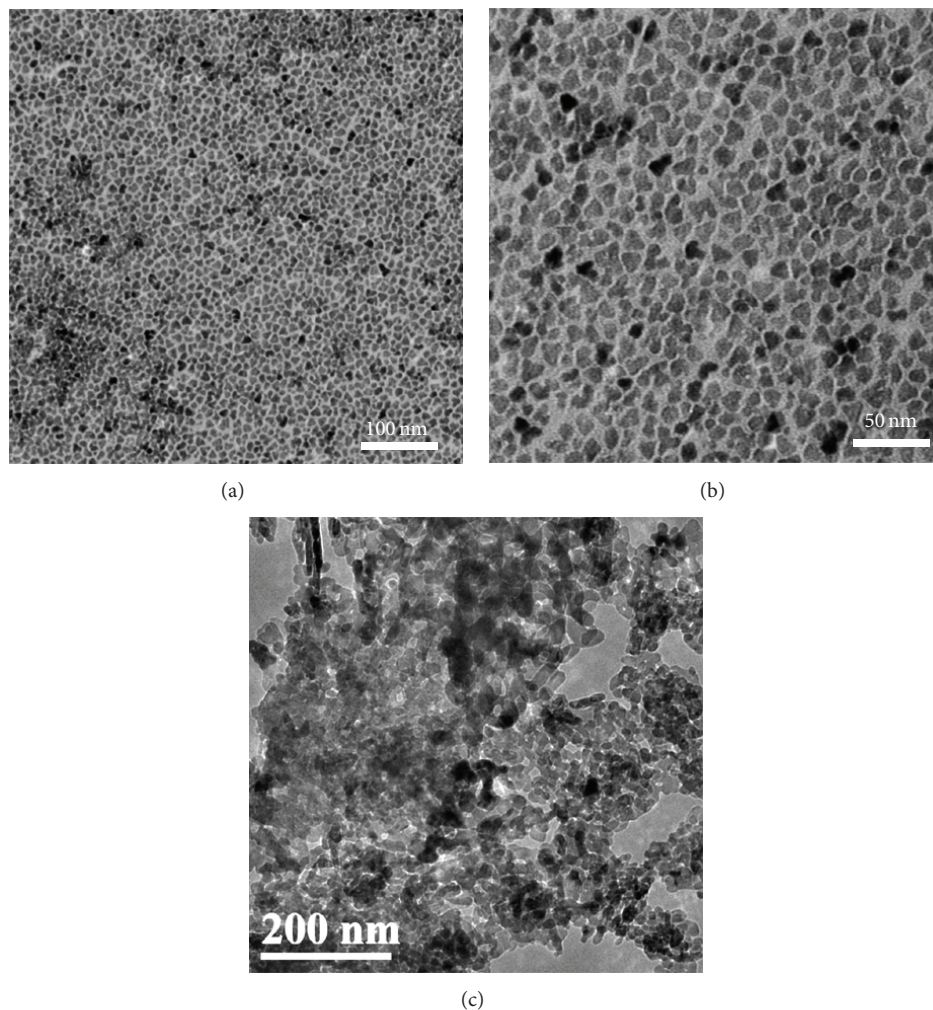


FIGURE 2: TEM images of (a, b) ZnO nanocrystals and (c) commercial ZnO nanoparticles.

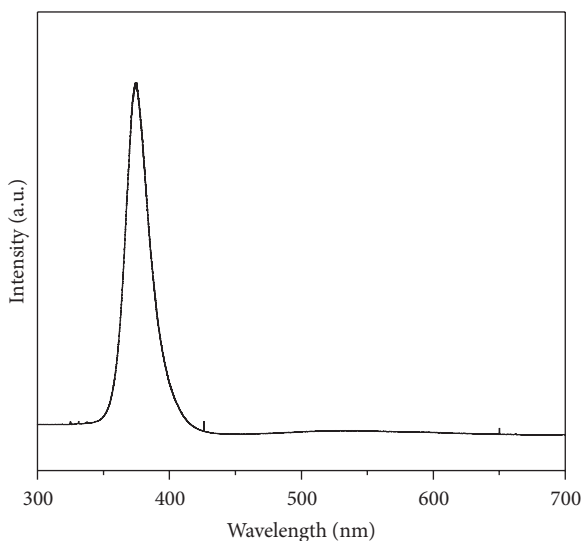


FIGURE 3: PL spectrum of ZnO nanocrystals.

of  $200 \text{ mA g}^{-1}$  and  $400 \text{ mA g}^{-1}$  were displayed in Figure 5. At  $200 \text{ mA g}^{-1}$ , ZnO nanocrystal electrode delivered a high initial charge/discharge capacity of  $709/1563 \text{ mAh g}^{-1}$  and exhibited a high average discharge capacity of  $500 \text{ mAh g}^{-1}$  over 100 cycles, while commercial ZnO nanoparticle electrode delivered a lower initial charge/discharge capacity of  $489/1273 \text{ mAh g}^{-1}$  and exhibited a lower average discharge capacity of  $112 \text{ mAh g}^{-1}$  over 100 cycles. At  $400 \text{ mA g}^{-1}$ , the electrodes showed similar results. The ZnO nanocrystal electrode displayed a better cycling performance, which delivered an initial charge/discharge capacity of  $676/1475 \text{ mAh g}^{-1}$  with a coulombic efficiency of 45.8% and exhibited the discharge capacity of  $428 \text{ mAh g}^{-1}$  over 100 cycles.

The rate capabilities of ZnO nanocrystal electrode are shown in Figure 6. ZnO nanocrystal electrode was cycled at a current density of  $200 \text{ mA g}^{-1}$  for the initial 2 cycles. Then, the current density was increased gradually to  $4000 \text{ mA g}^{-1}$  and finally returned to  $200 \text{ mA g}^{-1}$ . The ZnO nanocrystal

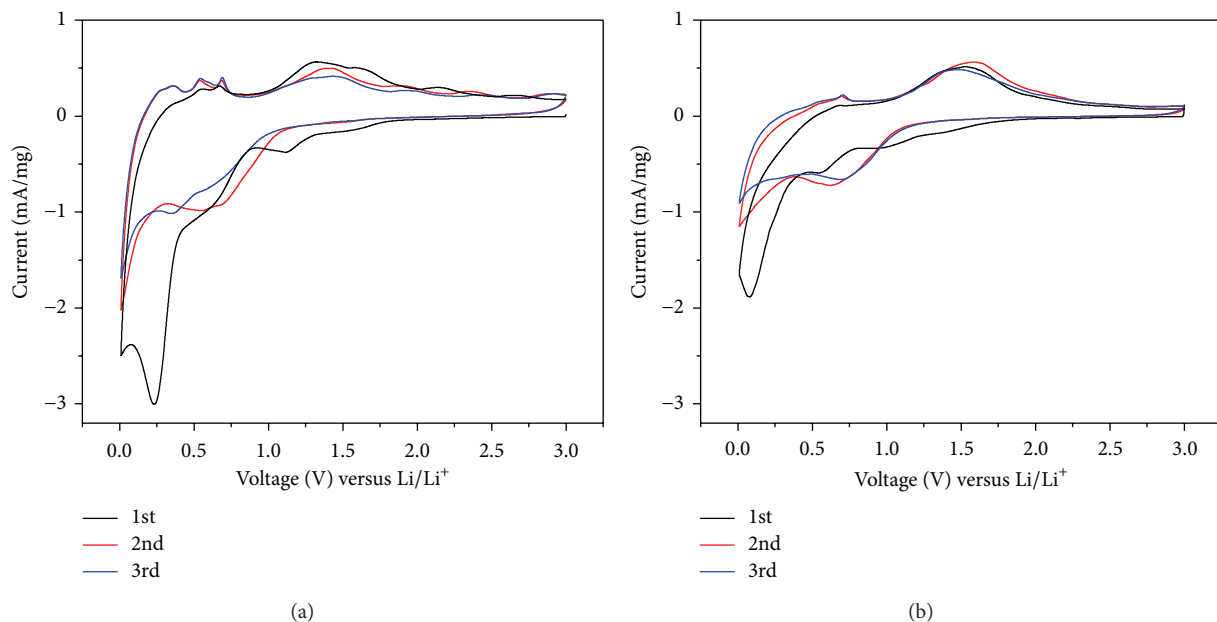


FIGURE 4: Cyclic voltammograms of (a) ZnO nanocrystal and (b) commercial ZnO nanoparticle electrode tested at  $0.5 \text{ mV s}^{-1}$  in 0.01–3 V.

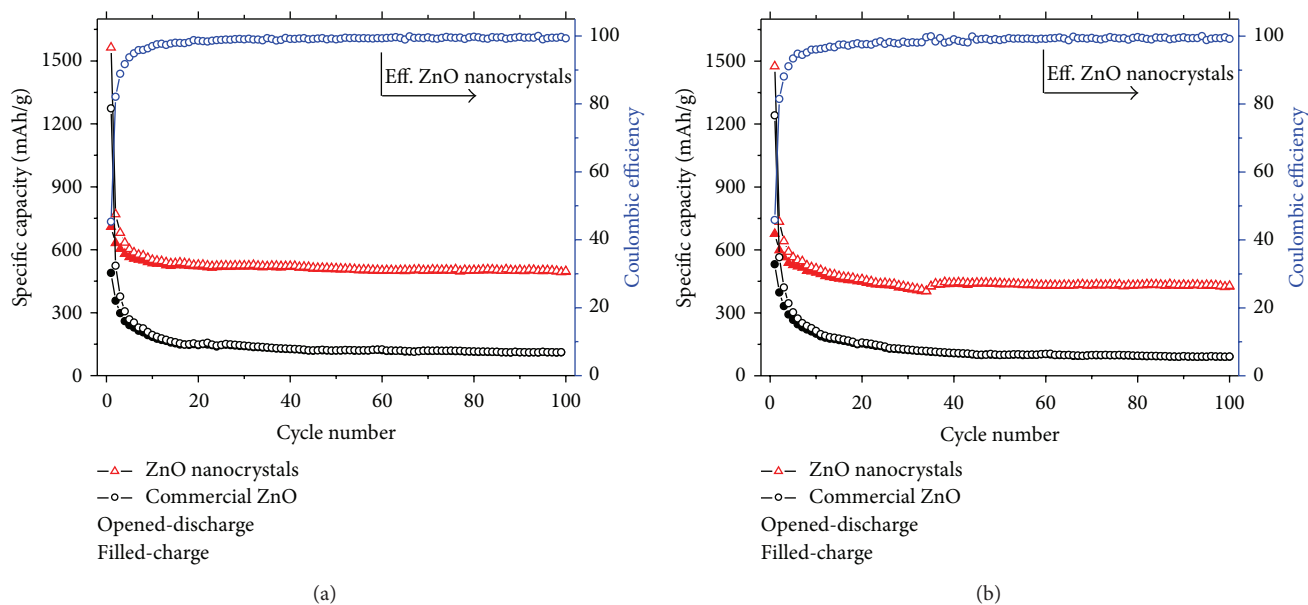


FIGURE 5: Cycle performances of ZnO nanocrystal and commercial ZnO nanoparticle electrode at a current density of (a)  $200 \text{ mA g}^{-1}$  and (b)  $400 \text{ mA g}^{-1}$ .

electrode showed a first charge/discharge capacity of  $570/1272 \text{ mAh g}^{-1}$  with a coulombic efficiency of 44.8%. At a higher current density of 500, 1000, 2000, 3000, and  $4000 \text{ mA g}^{-1}$ , the capacity dropped to about 309, 187, 114, 75, and  $51 \text{ mAh g}^{-1}$ , respectively.

To investigate the difference in electrochemical performance, EIS was employed to characterize the impedance properties of electrodes. The Nyquist complex plane impedance plots of the electrodes after the first two charge/discharge cyclic processes are presented in Figure 7. Both Nyquist plots

which consisted of a depressed semicircle at high frequency range correlated with the electron transfer resistance on the interface of electrode/electrolyte. These Nyquist plots were fitted with the equivalent circuit (inset), as shown in Figure 7. This equivalent circuit consisted of a series of four resistors elements, three constant-phase elements (CPE), and a Warburg diffusion element. In the equivalent circuit,  $R_1$  was composed of the electrolyte resistance ( $R_s$ ) and the electrode resistance ( $R_e$ );  $R_2$  represented the SEI film resistances;  $R_3$  represented the interphase electronic contacts

TABLE 1

Sample ID	$R_1$ ( $\Omega$ )	$R_2$ ( $\Omega$ )	$R_3$ ( $\Omega$ )	$R_4$ ( $\Omega$ )	CPE <sub>1</sub>		CPE <sub>2</sub>		CPE <sub>3</sub>		$W$ (DW)
					$Y_{0,1}$ ( $\mu\text{F}$ )	$n$	$Y_{0,2}$ ( $\mu\text{F}$ )	$n$	$Y_{0,3}$ ( $\mu\text{F}$ )	$n$	
Commercial ZnO	0.3	1.7	107.1	43.1	0.55	0.4	4.7	0.8	103.5	0.7	69.2
ZnO nanocrystals	0.3	1.3	53.4	22.2	0.91	0.4	6.2	0.6	280.5	0.6	47.6

$Y_0$  and  $n$  are two parameters of the constant-phase element.

TABLE 2: Electrochemical performance comparison of ZnO-based anodes for lithium-ion batteries.

The structure of the material	Specific discharge capacity ( $\text{mAh g}^{-1}$ )	Cycle number	Current density	References
ZnO radial hollow microparticles	320	100	$200 \text{ mA g}^{-1}$	[28]
ZnO nanowires	252	30	$120 \text{ mA g}^{-1}$	[29]
ZnO flower-like microaggregates	179	200	1 C	[30]
ZnO dandelion-like nanorod arrays	310	40	$250 \text{ mA g}^{-1}$	[27]
ZnO flower-like arrays	238	50	0.5 C	[31]
ZnO microrod arrays	150	50	$500 \text{ mA g}^{-1}$	[16]
ZnO nanowire arrays	200	40	$120 \text{ mA g}^{-1}$	[32]
ZnO flower-like microparticles	200	50	$120 \text{ mA g}^{-1}$	[33]
ZnO nanoplates	368	100	0.1 C	[34]
ZnO mesoporous nanosheets	420	50	$100 \text{ mA g}^{-1}$	[17]
Flower-like ZnO nanospheres	381	30	0.5 C	[35]
Ultralong mesoporous ZnO nanowires	432	10	0.1 C	[36]
ZnO nanocrystals	500	100	$200 \text{ mA g}^{-1}$	This work
	428		$400 \text{ mA g}^{-1}$	

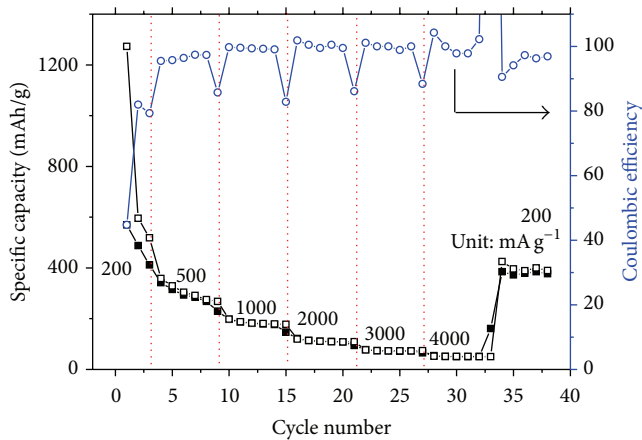


FIGURE 6: Rate performance of ZnO nanocrystal electrode.

resistance;  $R_4$  was the charge-transfer resistance across electrode/electrolyte interface; CPE<sub>1</sub> and CPE<sub>2</sub> were attributed to the  $\text{Li}^+$  diffusion in the SEI film and pore channel of the electrode materials, respectively; CPE<sub>3</sub> represented the electric double-layer capacitance of electrode/solution interface;  $Z_W$  which represented Warburg impedance was related to the semi-infinite diffusion of lithium ions into the bulk electrode [37, 38].

By fitting the impedance data, the typical parameters were obtained and summarized in Table 1. It was seen that the smaller  $R_3$  was also observed in ZnO nanocrystal electrode,

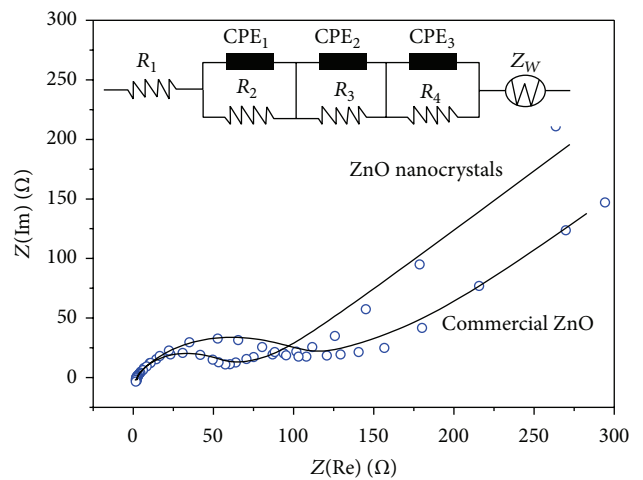


FIGURE 7: Nyquist plots for ZnO nanocrystal and commercial ZnO nanoparticle electrodes. The spots correspond to the experimental data, and the solid lines stand for the calculated data from the equivalent circuits of inset.

which usually favored the fast transport of  $\text{Li}^+$  ions and the electrons across the interface. It also indicated that the carbon layer supplied fast charge-transfer channels on the interface of ZnO nanocrystal.  $Y_{0,1}$ ,  $Y_{0,2}$ , and  $Y_{0,3}$  of the ZnO nanocrystal electrode were higher than those of commercial ZnO electrode. The increase of  $Y_{0,3}$  representing the electric double-layer capacitance favored the charge transfer for the

electrode reaction. And the increase of  $Y_{0,1}$  and  $Y_{0,2}$  favored the diffusion of  $\text{Li}^+$  in the SEI film and within the pore channels in the electrode, respectively.

ZnO nanocrystal electrode showed a smaller charge-transfer resistance and higher electric double-layer capacitance as compared with the commercial ZnO electrode, indicating an improved kinetic character of electrode reactions (i.e., charge transfer and polarization) which could be ascribed to the better availability of electrons and perhaps also  $\text{Li}^+$ . The smaller particle size and better crystal type constituted a fast pathway for mass transport and electron transfer and hence improved Li storage capacity. The excellent capacity of the ZnO nanocrystals is highly attractive when compared with other reported ZnO-based anode materials (Table 2).

#### 4. Conclusion

In summary, ZnO nanocrystals with side-edge length of 10–15 nm were synthesized via the thermal decomposition method. A high reversible discharge capacity of  $500 \text{ mAh g}^{-1}$  of ZnO nanocrystals was observed after 100 cycles at  $200 \text{ mA g}^{-1}$ . Compared with commercial ZnO nanoparticles, ZnO nanocrystals showed higher lithium storage capacity. These results are attributed to the structural difference of ZnO nanocrystals resulting in different cell impedance, which affects the Li-ion diffusion.

#### Competing Interests

The authors declare that there are no competing interests regarding the publication of this paper.

#### Acknowledgments

This study is supported by the National Natural Science Foundation of China (nos. 51402252 and 51541505) and the Natural Science Foundation of Jiangsu Province (no. BK20140463).

#### References

- [1] A. K. Mondal, D. Su, S. Chen, A. Ung, H.-S. Kim, and G. Wang, "Mesoporous  $\text{MnCo}_2\text{O}_4$  with a flake-like structure as advanced electrode materials for lithium-ion batteries and supercapacitors," *Chemistry—A European Journal*, vol. 21, no. 4, pp. 1526–1532, 2015.
- [2] N. N. Wang, X. J. Ma, H. Y. Xu et al., "Porous  $\text{ZnMn}_2\text{O}_4$  microspheres as a promising anode material for advanced lithium-ion batteries," *Nano Energy*, vol. 6, pp. 193–199, 2014.
- [3] W. Zhang, L. Yue, F. Zhang et al., "One-step in situ synthesis of ultrathin tungsten oxide@carbon nanowire webs as an anode material for high performance," *Journal of Materials Chemistry A*, vol. 3, no. 11, pp. 6102–6109, 2015.
- [4] Y. Zhu, C. Cao, J. Zhang, and X. Xu, "Two-dimensional ultrathin  $\text{ZnCo}_2\text{O}_4$  nanosheets: general formation and lithium storage application," *Journal of Materials Chemistry A*, vol. 3, no. 18, pp. 9556–9564, 2015.
- [5] C. F. Pan, R. M. Yu, S. M. Niu, G. Zhu, and Z. L. Wang, "Piezotronic effect on the sensitivity and signal level of schottky contacted proactive micro/nanowire nanosensors," *ACS Nano*, vol. 7, no. 2, pp. 1803–1810, 2013.
- [6] Y.-H. Tan, K. Yu, J.-Z. Li, H. Fu, and Z.-Q. Zhu, "MoS<sub>2</sub>@ZnO nano-heterojunctions with enhanced photocatalysis and field emission properties," *Journal of Applied Physics*, vol. 116, no. 6, Article ID 064305, 2014.
- [7] Y. D. Zhu, Y. Y. Wang, G. T. Duan et al., "In situ growth of porous ZnO nanosheet-built network film as high-performance gas sensor," *Sensors and Actuators B: Chemical*, vol. 221, Article ID 18692, pp. 350–356, 2015.
- [8] L. X. Song, P. F. Du, J. Xiong, F. Ko, and C. Cui, "Efficiency enhancement of dye-sensitized solar cells by optimization of electrospun ZnO nanowire/nanoparticle hybrid photoanode and combined modification," *Electrochimica Acta*, vol. 163, pp. 330–337, 2015.
- [9] Y. Wang, H. Fang, Y. Zheng, R. Ye, X. Tao, and J. Chen, "Controllable assembly of well-defined monodisperse Au nanoparticles on hierarchical ZnO microspheres for enhanced visible-light-driven photocatalytic and antibacterial activity," *Nanoscale*, vol. 7, no. 45, pp. 19118–19128, 2015.
- [10] Y. F. Yang, Y. Z. Jin, H. P. He et al., "Dopant-induced shape evolution of colloidal nanocrystals: the case of zinc oxide," *Journal of the American Chemical Society*, vol. 132, no. 38, pp. 13381–13394, 2010.
- [11] L. Nasi, D. Calestani, F. Fabbri et al., "Mesoporous single-crystal ZnO nanobelts: supported preparation and patterning," *Nanoscale*, vol. 5, no. 3, pp. 1060–1066, 2013.
- [12] Y.-J. Wu, C.-H. Liao, C.-Y. Hsieh et al., "Local electronic structures and polarity of ZnO nanorods grown on GaN substrates," *Journal of Physical Chemistry C*, vol. 119, no. 9, pp. 5122–5128, 2015.
- [13] A. Umar, M. S. Akhtar, M. S. Al-Assiri et al., "Highly porous ZnO nanosheets self-assembled in rosette-like morphologies for dye-sensitized solar cell application," *New Journal of Chemistry*, vol. 39, no. 10, pp. 7961–7970, 2015.
- [14] Q. Pan, L. Qin, J. Liu, and H. Wang, "Flower-like ZnO-NiO-C films with high reversible capacity and rate capability for lithium-ion batteries," *Electrochimica Acta*, vol. 55, no. 20, pp. 5780–5785, 2010.
- [15] X. H. Huang, X. H. Xia, Y. F. Yuan, and F. Zhou, "Porous ZnO nanosheets grown on copper substrates as anodes for lithium ion batteries," *Electrochimica Acta*, vol. 56, no. 14, pp. 4960–4965, 2011.
- [16] X. H. Huang, J. B. Wu, Y. Lin, and R. Q. Guo, "ZnO microrod arrays grown on copper substrates as anode materials for lithium ion batteries," *International Journal of Electrochemical Science*, vol. 7, no. 8, pp. 6611–6621, 2012.
- [17] X. H. Huang, R. Q. Guo, J. B. Wu, and P. Zhang, "Mesoporous ZnO nanosheets for lithium ion batteries," *Materials Letters*, vol. 122, pp. 82–85, 2014.
- [18] L. F. Zhang, J. Z. Zhang, Y. Liu, P. Zheng, X. Y. Yuan, and S. W. Guo, "Al doped-ZnO nanoparticles implanted in reduced graphene oxide with improved electrochemical properties for lithium ion batteries," *Materials Letters*, vol. 165, pp. 165–168, 2016.
- [19] X. Shen, D. Mu, S. Chen, R. Huang, and F. Wu, "Electrospun composite of ZnO/Cu nanocrystals-implanted carbon fibers as an anode material with high rate capability for lithium ion batteries," *Journal of Materials Chemistry A*, vol. 2, no. 12, pp. 4309–4315, 2014.
- [20] M. S. Song, S. Nahm, W. I. Cho, and C. Lee, "Enhanced electrochemical performance of a ZnO-MnO composite as an anode

- material for lithium ion batteries,” *Physical Chemistry Chemical Physics*, vol. 17, no. 36, pp. 23496–23502, 2015.
- [21] Y. Zhao, X. Li, L. Dong et al., “Electrospun SnO<sub>2</sub>-ZnO nanofibers with improved electrochemical performance as anode materials for lithium-ion batteries,” *International Journal of Hydrogen Energy*, vol. 40, no. 41, pp. 14338–14344, 2015.
- [22] C. Y. Zhang, J. Dai, P. G. Zhang et al., “Porous Fe<sub>2</sub>O<sub>3</sub>/ZnO composite derived from MOFs as an anode material for lithium ion batteries,” *Ceramics International*, vol. 42, no. 1, pp. 1044–1049, 2016.
- [23] Y. Xiao and M. Cao, “Dual hybrid strategy towards achieving high capacity and long-life lithium storage of ZnO,” *Journal of Power Sources*, vol. 305, pp. 1–9, 2016.
- [24] G. Zhang, S. Hou, H. Zhang et al., “High-performance and ultra-stable lithium-ion batteries based on MOF-derived ZnO@ZnO quantum dots/C core-shell nanorod arrays on a carbon cloth anode,” *Advanced Materials*, vol. 27, no. 14, pp. 2400–2405, 2015.
- [25] X. Sun, C. Zhou, M. Xie et al., “Synthesis of ZnO quantum dot/graphene nanocomposites by atomic layer deposition with high lithium storage capacity,” *Journal of Materials Chemistry A*, vol. 2, no. 20, pp. 7319–7326, 2014.
- [26] C.-T. Hsieh, C.-Y. Lin, Y.-F. Chen, and J.-S. Lin, “Synthesis of ZnO@Graphene composites as anode materials for lithium ion batteries,” *Electrochimica Acta*, vol. 111, pp. 359–365, 2013.
- [27] H. Wang, Q. Pan, Y. Cheng, J. Zhao, and G. Yin, “Evaluation of ZnO nanorod arrays with dandelion-like morphology as negative electrodes for lithium-ion batteries,” *Electrochimica Acta*, vol. 54, no. 10, pp. 2851–2855, 2009.
- [28] G. Yuan, G. Wang, H. Wang, and J. Bai, “Synthesis and electrochemical investigation of radial ZnO microparticles as anode materials for lithium-ion batteries,” *Ionics*, vol. 21, no. 2, pp. 365–371, 2015.
- [29] J. Wang, N. Du, H. Zhang, J. Yu, and D. Yang, “Layer-by-layer assembly synthesis of ZnO/SnO<sub>2</sub> composite nanowire arrays as high-performance anode for lithium-ion batteries,” *Materials Research Bulletin*, vol. 46, no. 12, pp. 2378–2384, 2011.
- [30] V. Cauda, D. Pugliese, N. Garino et al., “Multi-functional energy conversion and storage electrodes using flower-like Zinc oxide nanostructures,” *Energy*, vol. 65, pp. 639–646, 2014.
- [31] Z. Wu, L. Qin, and Q. Pan, “Fabrication and electrochemical behavior of flower-like ZnO-CoO-C nanowall arrays as anodes for lithium-ion batteries,” *Journal of Alloys and Compounds*, vol. 509, no. 37, pp. 9207–9213, 2011.
- [32] M. Ahmad, S. Yingying, H. Sun, W. C. Shen, and J. Zhu, “SnO<sub>2</sub>/ZnO composite structure for the lithium-ion battery electrode,” *Journal of Solid State Chemistry*, vol. 196, pp. 326–331, 2012.
- [33] M. Ahmad, S. Yingying, A. Nisar et al., “Synthesis of hierarchical flower-like ZnO nanostructures and their functionalization by Au nanoparticles for improved photocatalytic and high performance Li-ion battery anodes,” *Journal of Materials Chemistry*, vol. 21, no. 21, pp. 7723–7729, 2011.
- [34] H. Li, Y. Wei, Y. Zhao et al., “Simple one-pot synthesis of hexagonal ZnO nanoplates as anode material for lithium-ion batteries,” *Journal of Nanomaterials*, vol. 2016, Article ID 4675960, 6 pages, 2016.
- [35] F. Li, L. L. Yang, G. Xu et al., “Hydrothermal self-assembly of hierarchical flower-like ZnO nanospheres with nanosheets and their application in Li-ion batteries,” *Journal of Alloys and Compounds*, vol. 577, pp. 663–668, 2013.
- [36] H.-J. Yang, S.-C. Lim, S.-Y. He, and H.-Y. Tuan, “Ultralong mesoporous ZnO nanowires grown via room temperature self-assembly of ZnO nanoparticles for enhanced reversible storage in lithium ion batteries,” *RSC Advances*, vol. 5, no. 42, pp. 33392–33399, 2015.
- [37] L. Yue, W. Zhang, W. Zhang et al., “One-step solvothermal process of In<sub>2</sub>O<sub>3</sub>/C nanosheet composite with double phases as high-performance lithium-ion battery anode,” *Electrochimica Acta*, vol. 160, pp. 123–130, 2015.
- [38] W. Zhang, L. Wu, L. Du et al., “Layer-by-layer assembly modification to prepare firmly bonded Si-graphene composites for high-performance anodes,” *RSC Advances*, vol. 6, no. 6, pp. 4835–4842, 2016.



**Hindawi**

Submit your manuscripts at  
<http://www.hindawi.com>

